A Digital Internal Model Current Controller for Salient Machines

Ivan Z. Petric, *Student Member, IEEE*, Slobodan N. Vukosavic, *Senior Member, IEEE*, Michele Degano, *Member, IEEE*, and Alessandro Galassini, *Member, IEEE*

***Abstract*—The performance of anisotropic electrical machines is strongly dependent on the current loop characteristics. The problems for achieving robustness and fast response, without overshoot and oscillations, are mainly related to different values and behaviour of the direct and quadrature inductances (L_d, L_q), as well as to high output frequencies. In this paper, a novel current controller structure based on Internal Model Control (IMC) method is presented, taking into account the magnetic anisotropy ($L_d \neq L_q$). The model of salient machines is derived directly in the discrete domain and used to obtain a model-based controller. The controller derivation does not rely on transport-delay approximations, which enables improved decoupling of axes dynamics and the closed-loop robustness for very high output frequencies. The presented controller enables enhanced response for higher current loop bandwidth and output frequencies than the state-of-the-art methods. The experimental verification is performed on a 3-phase synchronous machine, using a standard industrial 3-phase inverter.**

***Index Terms*—Digital Current Control, Internal Model Control, Salient Machines, Synchronous Machines, Synchronous Reluctance.**

I. Introduction

CURRENT control system is the basis of the field-oriented control (FOC) of electrical drives. Out of many possible strategies for designing a current controller [1]–[3], the ones most widely used are PI controllers implemented in the synchronous rotating frame [4]–[7], as they provide satisfactory performance over a wide frequency range [4]. Further improvements are obtained by applying the Internal Model Control (IMC) method [5], where the only design parameter is the closed-loop bandwidth. Transport-delay approximations in S-domain based designs [6]–[10] prove insufficient when it comes to large bandwidth to sampling $\frac{f_{bw}}{f_s}$ and output to sampling $\frac{f_{out}}{f_s}$ frequency ratios. Therefore, high-performance controllers are directly derived in discrete-time domain, without any approximations [11]–[17]. By following that approach, axes decoupling is inherently found in the controller structure, and the reported closed-loop f_{bw} for a current step response without overshoot, exceeds $17\%f_s$ [16].

The complex notation [8], [9] greatly simplifies the model statement and the design steps, yet, it cannot be applied in cases where the parameters in perpendicular axes are different ($L_d \neq L_q$). Recently, significant attention was dedicated to salient electrical machines, especially for automotive applications [18]–[20]. The high-performance Interior Permanent Magnet Synchronous Machines (IPMSM) have a very high torque density and wide speed operating range. Another popular type of salient machines are Synchronous Reluctance (SynRel) and Permanent Magnet assisted Synchronous Reluctance (PMaSynRel), which are promising candidates with respect to induction machines, thanks to their simplified production process and reduced rotor iron losses [21]. Digital current controllers for salient machines have to provide high bandwidth and decoupled response even in cases with considerable differences between L_d and L_q, and for high output frequencies. High current loop bandwidths enable a fast torque response, which is crucial for the performance of outer speed and position loops. A possible solution is the implementation of predictive control strategies [22]–[24], which are capable of providing a fast response. However, in terms of robustness, the predictive control is very sensitive to parameter mismatch, and IMC methods provide better stability margins, which is preferred in industrial applications. Several authors [10], [11], [13], [25], [26] have dedicated their attention to current controller design for salient machines, which led to the following results. In [10], the controller derivation is not clearly stated and the authors report the $f_{bw} = 3\%f_s$. In [25], the authors use a combination of strategies that deal with saliency in the continuous-time domain, and controller derivation in discrete-time domain. In that paper, the proposed controller is very similar to discrete IMC for non-salient machines [12], [15]–[17]. However, from the presented results, it can be seen that the method from [25] is not capable of fully decoupling the axes dynamics. The exact discrete state-space model of salient machines can be seen in [11] and [13]. The results of [11] are shown only for a machine with $L_d \approx L_q$, without many details. The paper [13] does not present a practical controller structure due to the complicated system matrices. The presented results cover only for a very low sampling frequency, using a powerful dSPACE platform. It is not clear how effective this can be in standard industrial applications that use lower cost DSP platforms. In [13], the experimental

Manuscript received September 5, 2019; revised January 2, 2020 and March 15, 2020; accepted April 4, 2020. This work was supported by the project F-143 of the Serbian Academy of Sciences and Arts. (Corresponding author: Ivan Petric.)

I. Z. Petric is with the Department of Information Engineering, The University of Padova, Padova, 35131, Italy (e-mail: petric@dei.unipd.it).

S. N. Vukosavic is with the Department of Electrical Engineering, The University of Belgrade, Belgrade, 11000, Serbia, and Serbian Academy of Sciences and Arts (e-mail: boban@etf.rs).

M. Degano and A. Galassini are with the PEMC Group, Department of Electrical and Electronic Engineering, The University of Nottingham, NG7 2RD, Nottingham, United Kingdom (e-mail: michele.degano@nottingham.ac.uk, alessandro.galassini@nottingham.ac.uk).

M. Degano is also with the Key Laboratory of More Electric Aircraft Technology of Zhejiang Province, PEMC Group, University of Nottingham Ningbo Campus, UNNC, China.

results are given for a SynRel machine and the reported closed-loop bandwidth is $f_{bw} = 5\%f_s$ for output frequencies up to $f_{out} = 10\%f_s$. An interesting approach is presented in [26], where the IMC method is used in the complex form, for a plant with neglected stator resistance. The experimental results in [26] report $f_{bw} \approx 7\%f_s$ for output frequencies up to $f_{out} \approx 12\%f_s$.

This paper offers a novel structure for digital current controller, suitable for salient machines. The motivation is to derive a discrete IMC with a simplified structure compared to [13], enabling its practical use in industrial applications. The proposed controller retains robustness at high output frequencies and offers high bandwidth and stability margins. The first step is to derive a precise direct-discrete model of salient machines, simplified compared to [11] and [13]. The simplifications are thoroughly analyzed in order to ensure robustness for very high output frequencies and values of machine saliency. The obtained model is used to derive the model-based controller structure. The frequency response analysis of the current loop is performed in order to validate the modeling approximations. The experimental results show improved current response compared to the state-of-the-art methods. The experimental results are provided for output frequency ratios up to $\frac{f_{out}}{f_s} = 18\%$, with the relative current loop bandwidth equal to $\frac{f_{bw}}{f_s} = 12.2\%$.

The paper is organized as follows: section II presents derivations of the discrete-time model of salient machines and the structure of the model-based digital controller. The analysis of modeling approximations is shown in section III. In section IV, the closed-loop system is analyzed, and the controller is designed according to the desired bandwidth, overshoot, and stability vector margin. Simulations are used to show the current loop frequency response analysis and step responses, which confirm the model accuracy for very high output frequencies and values of machine saliency. The experimental results and comparison with the state-of-the-art methods are shown in section V. Section VI summarizes the conclusions of the study, highlighting the effectiveness of the proposed method.

For clarity purposes, all matrices are labelled in bold font.

II. Machine Modeling and Controller Derivation

In this section, the discrete-time model of salient machines is derived. Depending on whether the machine current [10]–[12], [15]–[17], [27] or flux [13], [26] is chosen as a state variable, two different models can be derived. The demerit of using currents as state variables is the introduction of differential inductances in the mathematical model [27]. In the flux model, all saturation and cross-saturation effects are inherently taken into account, which is especially important for highly nonlinear machines, such as SynRel or PMaSynRel. Contrary to non-salient machines [12], [15]–[17], the plant model for machines with $L_d \neq L_q$ can not be represented in the complex form, which makes the structure more complicated. The model derived in subsection II A has a significantly simplified structure compared to [11] and [13], yet retains the high accuracy. The model-based flux controller is subsequently derived in subsection II B.

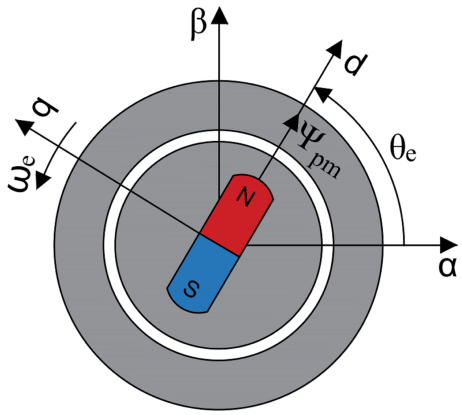

Fig. 1: Synchronous machine axes convention.

A. The discrete-time model of salient machines

The discrete-time model for machines with $L_d \neq L_q$ is derived using the state-space matrix representation. The stator flux is chosen as the state variable as it is more appropriate for machines with magnetic saturation. For the chosen axes convention, shown in Fig. 1, the dq voltage equations of synchronous machines are:

$$\begin{aligned} u_d &= Ri_d + \frac{d\Psi_d}{dt} - \omega_e \Psi_q \\ u_q &= Ri_q + \frac{d\Psi_q}{dt} + \omega_e \Psi_d, \end{aligned} \tag{1}$$

where u_d and u_q are the dq axes voltages, R is the stator winding resistance, and ω_e is the electrical rotational speed.

The total flux in the d axis is equal to $\Psi_d = L_d i_d + \Psi_{pm}$, where Ψ_{pm} is the permanent magnet flux. The total flux in the q axis is equal to $\Psi_q = L_q i_q$. The following substitution is introduced: $F_d = L_d i_d$, $F_q = L_q i_q$. This is done to separate the flux contribution resulting from the permanent magnet and the one related to the current bias. The permanent magnet flux is considered to be a slow-changing external disturbance ($\frac{d\Psi_{pm}}{dt} = 0$). Based on (1) and the discussion above, the following continuous-time state-space model is obtained:

$$\begin{aligned} &\frac{\mathrm{d}}{\mathrm{dt}}\mathbf{F} = \mathbf{A}\cdot\mathbf{F} + \mathbf{I}\cdot\mathbf{u} - \begin{bmatrix} 0 \\ \omega_e \end{bmatrix} \Psi_{pm} \\ &\mathbf{F} = \begin{bmatrix} L_d i_d \\ L_q i_q \end{bmatrix} \qquad \mathbf{u} = \begin{bmatrix} u_d \\ u_q \end{bmatrix} \\ &\mathbf{I} = \begin{bmatrix} 1 & 0 \\ 0 & 1 \end{bmatrix} \qquad \mathbf{A} = \begin{bmatrix} -\frac{R}{L_d} & \omega_e \\ -\omega_e & -\frac{R}{L_q} \end{bmatrix} \end{aligned} \tag{2}$$

High-performance digital current controllers are derived directly in the discrete-time domain, without any transport-delay approximations. For this, the precise sampling and control instants must be taken into account in the process of the model derivation. The sampling and control action time scheduling is shown in Fig. 2. In this paper, the synchronous double sampling is used, where the PWM duty cycle is set twice per PWM period ($T_{pwm} = 2T_s$). The current feedback vector is acquired at the moment $(n-1)T_s$ and transformed to the flux vector $\mathbf{F}_{n-1}$, which is used to calculate the voltage

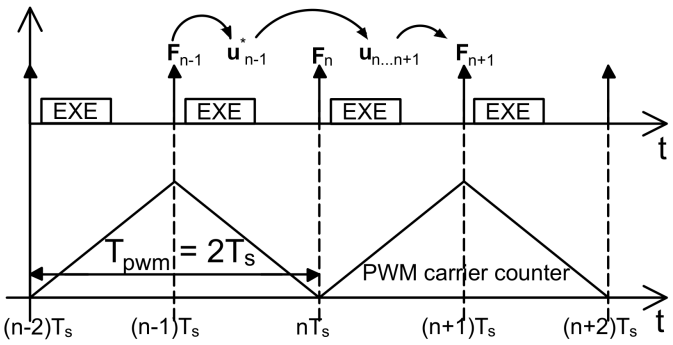

Fig. 2: Time schedule for sampling and control actions.

reference vector $\mathbf{u}^*_{n-1}$. The resulting voltage vector $\mathbf{u}_{n...n+1}$ is applied in the next sampling instant nT_s. With disregard of the external disturbance Ψ_{pm}, the solution of the matrix differential equation (2) is used to form a matrix difference equation, relative to the time schedule shown in Fig. 2:

$$\mathbf{F}_{n+1} = e^{\mathbf{A}T_s} \cdot \mathbf{F}_n - \left(\mathbf{I} - e^{\mathbf{A}T_s}\right) \cdot \mathbf{A}^{-1} \cdot \mathbf{u}_{n...n+1} \tag{3}$$

The matrix $e^{\mathbf{A}T_s}$ is calculated using the *Putzer Algorithm* for matrix exponential:

$$e^{\mathbf{A}T_s} = e^{-\sigma T_s} \begin{bmatrix} \cosh(\lambda T_s) - \delta\frac{\sinh(\lambda T_s)}{\lambda} & \omega_e\frac{\sinh(\lambda T_s)}{\lambda} \\ -\omega_e\frac{\sinh(\lambda T_s)}{\lambda} & \cosh(\lambda T_s) + \delta\frac{\sinh(\lambda T_s)}{\lambda} \end{bmatrix}, \tag{4}$$

where

$$\sigma = \frac{R}{2}\left(\frac{1}{L_d} + \frac{1}{L_q}\right), \quad \delta = \frac{R}{2}\left(\frac{1}{L_d} - \frac{1}{L_q}\right), \quad \lambda = \sqrt{\delta^2 - \omega_e^2} \tag{5}$$

Note that equation (3) strictly holds if and only if the applied voltage $\mathbf{u}_{n...n+1}$ is latched in dq frame, during the analyzed control period (if the zero-order hold (ZOH) is assumed to be in the synchronous frame). In the physical domain, the inverter output voltage can be latched only in stationary $\alpha\beta$ frame, which makes the output voltage time-variant in dq frame during the analyzed control period [19]. The modeling of non-salient machines with ZOH assumed in the synchronous frame can be seen in [28], and it results in gain and angle errors that need to be compensated. The discrete modeling of salient machines that assumes the ZOH in the stationary frame can be seen in [11], [13], [19]. The approximation of the ZOH being in the synchronous frame, by analogy with the approach in [28], yields a much simpler model of salient machines, which is crucial for the derivation of the proposed IMC structure. This simplification is analyzed in subsection III A, where it is shown that it does not have a significant impact on the model accuracy. This is also confirmed by the results of frequency response analysis in subsection IV B.

In (3), the value of the applied voltage vector $\mathbf{u}_{n...n+1}$ is not equal to the set reference vector $\mathbf{u}^*_{n-1}$, due to the dq frame rotation. During the period $[n...n+1]T_s$, the applied voltage vector is constant in the $\alpha\beta$ frame as the output of the voltage source inverter. Throughout the analyzed sampling period, the dq frame rotates, which leads to a distortion of the applied dq voltage, compared to the set reference value. Using the synchronous frame ZOH approximation, by analogy with [28], the imposed voltage vector features scalar error equal to $\frac{\frac{1}{2}\omega_e T_s}{\sin(\frac{1}{2}\omega_e T_s)}$ and angle error equal to $\frac{3}{2}\omega_e T_s$. In this paper, the scalar error is not compensated, and the ZOH is modeled as a phase delay. This approximation is validated in subsection III A. The connection between the applied dq voltage vector $\mathbf{u}_{n...n+1}$ and the reference vector $\mathbf{u}^*_{n-1}$ is modeled as:

$$\mathbf{u}_{n...n+1} = \mathbf{e}^{-j\frac{3}{2}\omega_e T_s} \cdot \mathbf{u}^*_{n-1}, \tag{6}$$

where $\mathbf{e}^{j\Theta} = \begin{bmatrix} \cos\Theta & \sin\Theta \\ -\sin\Theta & \cos\Theta \end{bmatrix}$ is the adopted notation for the matrix that rotates the vector by angle Θ, in the direction of the dq frame rotation.

Using (6), the matrix difference equation (3) is transformed into Z-domain:

$$z\mathbf{F}(z) = e^{\mathbf{A}T_s} \cdot \mathbf{F}(z) - z^{-1}\left(\mathbf{I} - e^{\mathbf{A}T_s}\right) \cdot \mathbf{A}^{-1} \cdot \mathbf{e}^{-j\frac{3}{2}\omega_e T_s} \cdot \mathbf{u}^*(z) \tag{7}$$

Since the IMC flux controller is obtained from the Z-domain matrix equation (7), it is of interest to simplify it, without significantly impacting the accuracy of the model. It is convenient to simplify (4) so that it is less dependent on ω_e and so that it features sinusoidal instead of hyperbolic functions. The assumption that transforms hyperbolic into sinusoidal functions is $\omega_e^2 >> \delta^2$. This approximation transforms λ into $j\omega_e$ and (4) into:

$$e^{\mathbf{A}T_s} \approx e^{-\sigma T_s} \begin{bmatrix} \cos(\omega_e T_s) - \delta\frac{\sin(\omega_e T_s)}{\omega_e} & \sin(\omega_e T_s) \\ -\sin(\omega_e T_s) & \cos(\omega_e T_s) + \delta\frac{\sin(\omega_e T_s)}{\omega_e} \end{bmatrix} \tag{8}$$

It is shown in subsection III B and subsection IV B that this approximation does not deteriorate the model accuracy even for output frequency equal to zero. In order to avoid division with small numbers in the low-speed region, the linear approximation $\frac{\sin(\omega_e T_s)}{\omega_e} \approx \frac{\omega_e T_s}{\omega_e} = T_s$ is used to transform (8) into the final matrix $\mathbf{E}$:

$$\mathbf{E} = e^{-\sigma T_s} \begin{bmatrix} \cos(\omega_e T_s) - \delta T_s & \sin(\omega_e T_s) \\ -\sin(\omega_e T_s) & \cos(\omega_e T_s) + \delta T_s \end{bmatrix} \tag{9}$$

This linear approximation is analyzed in subsection III C. As the outcome of using $\mathbf{E}$ instead of $e^{\mathbf{A}T_s}$, the difference equation (7) is simplified by eliminating the hyperbolic functions, as well as by significantly reducing the number of components that depend on the output frequency. The Z-domain transfer matrix $\mathbf{G}_{plant}(z)$ is introduced as:

$$\begin{aligned} &\mathbf{F}(z) = \mathbf{G}_{plant}(z) \cdot \mathbf{u}^*(z) \\ &\mathbf{G}_{plant}(z) = -z^{-1}\left(z\mathbf{I} - \mathbf{E}\right)^{-1} \cdot (\mathbf{I} - \mathbf{E}) \cdot \mathbf{A}^{-1} \cdot \mathbf{e}^{-j\frac{3}{2}\omega_e T_s} \end{aligned} \tag{10}$$

B. Derivation of the model-based flux controller

The field-oriented control system of a synchronous machine is shown in Fig. 3. It consists of current or flux references that are set by the outer control loops, flux or current controller, reference frame transformations, pulse-width modulator and inverter, synchronous machine, position estimator, and feedback

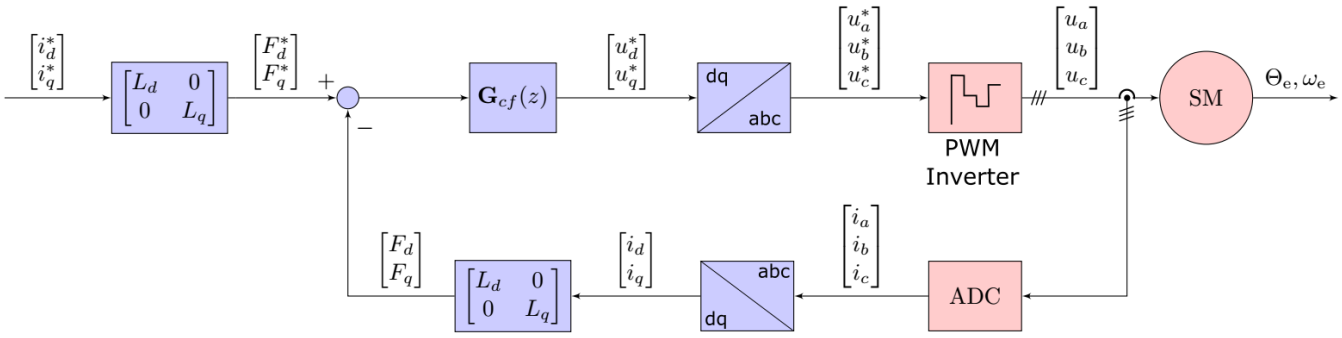

Fig. 3: The block diagram of a FOC system with currents as references and measurements.

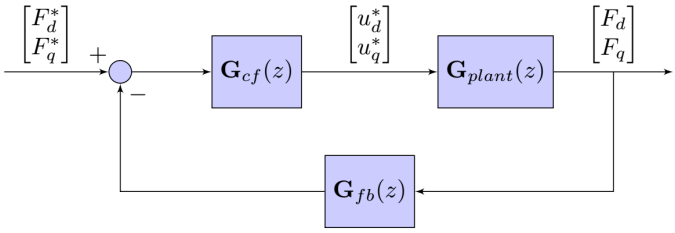

Fig. 4: The small-signal block diagram of a digital flux control system. For synchronous sampling, $\mathbf{G}_{fb}(z)$ is equal to the identity matrix $\mathbf{I}$.

acquisition system. In standard electric drive applications, line currents are available for sensing. In order to use the proposed flux model-based controller, current vectors are multiplied by the inductance matrix, and therefore transformed to the flux vectors. This corresponds to the transformation of a current control system into a flux control system. The small-signal block diagram of a digital flux control system is shown in Fig. 4.

As proposed in [5], the IMC concept consists of inverting the plant model and adding an integrator with a gain α that determines the closed-loop bandwidth. In digital applications, due to delays, an additional factor of $\frac{1}{z^2}$ must be added, in order to make a feasible controller without prediction [12]. The structure of the model-based flux controller is derived using (10):

$$\mathbf{G}_{cf}(z) = \alpha \frac{z}{z-1} \frac{1}{z^2} \mathbf{G}_{plant}^{-1}(z) \tag{11}$$

The derivation of the flux controller structure, based on the plant transfer matrix is given in Appendix A. The complete matrix form of the proposed flux controller is shown in (12), and its block diagram is presented in Fig. 5.

III. Analysis of Modeling Approximations

The matrix transfer function of salient machines (10), derived in the previous chapter, relies on several approximations. The exact direct-discrete model, derived in [13], has a very complicated structure, which is a result of matrix exponential terms and stationary frame ZOH. That model is very useful for analysis of salient machines, but it is not practical for the IMC design. In this paper, the model is simplified with the motivation to derive a compact controller structure that enables robust operation for high output frequencies and machines with high values of saliency. This section presents the analysis of the following modeling approximations, used in section II:

- The synchronous frame ZOH approximation, used in equations (3) and (6). This is a key approximation used in this paper, as it greatly reduces the structural complexity of the model.
- Transformation of (4) into (8): the approximation that transforms λ into $j\omega_e$. This approximation reduces the computational effort and transforms hyperbolical into sinusoidal functions.
- Transformation of (8) into (9): the first-order approximation of $\sin(\omega_e T_s)$ with $\omega_e T_s$. This approximation reduces the computational effort by removing the $sinc$ function.

The model sensitivity to these approximations is analyzed for a wide range of output to sampling frequency ratios and for machines with different values of saliency. The machines used for the analysis are described in Appendix B.A and Appendix B.B. The sensitivity analysis results are given for the sampling frequency of 20 kHz, to be consistent with the later simulations and experimental results.

A. The synchronous frame ZOH approximation

The inverter output voltage can be considered as piecewise constant between two sampling periods only in stationary $\alpha\beta$ frame. For non-salient machines, the discrete model is usually

The complete transfer matrix of the proposed flux controller

$$\mathbf{G}_{cf}(z) = \frac{\alpha}{\xi} \frac{z}{z-1} \mathbf{e}^{j\frac{3}{2}\omega_e T_s} \cdot (-\mathbf{A}) \cdot \left[e^{\sigma T_s} \mathbf{I} - \mathbf{e}^{j\omega_e T_s} + z^{-1} \left((1 - T_s^2 \delta^2) e^{-\sigma T_s} \mathbf{I} - \mathbf{e}^{-j\omega_e T_s} \right) + T_s \delta \begin{bmatrix} -1 & 0 \\ 0 & 1 \end{bmatrix} (1 - z^{-1}) \right] \tag{12}$$

$$\xi = e^{-\sigma T_s} \left(\omega_e^2 + \frac{R^2}{L_d L_q} \right) T_s^2$$

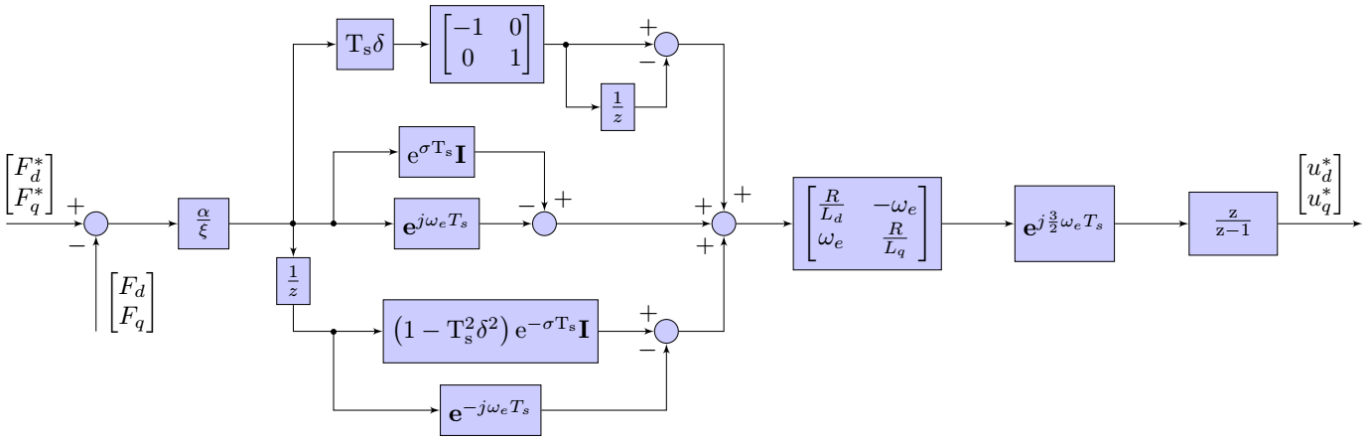

Fig. 5: The matrix block diagram of the proposed flux controller $\mathbf{G}_{cf}$.

derived starting from $\alpha\beta$ frame and then transformed into dq frame [15]. For salient machines, it is much easier to start from dq frame, as the inductance matrix in $\alpha\beta$ frame is dependent on the rotor position. Still, the direct derivation in dq frame yields a problem of modeling the equivalent applied voltage vector. In equation (3), the voltage vector $\mathbf{u}_{n\ldots n+1}$ is assumed to be latched in dq frame during the analyzed control period. The exact solution of the matrix differential equation (2) in discrete sampling instants is:

$$\mathbf{F}_{n+1} = e^{\mathbf{A}T_s} \cdot \mathbf{F}_n + \mathbf{B}(\omega_e, T_s, \delta, \sigma) \cdot \mathbf{e}^{-j\omega_e T_s} \cdot \mathbf{u}^*_{n-1} \quad , \quad (13)$$

where $\mathbf{B} = \int_0^{T_s} e^{\mathbf{A}t}\mathbf{e}^{-j\omega_e(T_s-t)}dt$ is the matrix that takes into account the stationary frame ZOH. The solution of $\mathbf{B}$ can be found in [13], where it is used to obtain the exact direct-discrete model. The solution of matrix $\mathbf{B}$ is very complicated on its own, even without inverting it, which is required to obtain the internal model controller (11). Therefore, it is of interest to simplify it by using the one-period synchronous frame latch assumption. For non-salient machines, the synchronous frame ZOH assumption introduces a scalar gain error and an angle error. A similar form is mentioned in [13] as a possible approximation, but this was not thoroughly analyzed.

In this paper, the connection between the applied and the reference voltage vectors is modeled as a phase delay equal to $\frac{3}{2}\omega_e T_s$. For a more precise modeling, the scalar gain error can also be included to obtain the same form shown in [28]:

$$\mathbf{u}_{n\ldots n+1} = \frac{\frac{1}{2}\omega_e T_s}{\sin(\frac{1}{2}\omega_e T_s)}\mathbf{e}^{-j\frac{3}{2}\omega_e T_s} \cdot \mathbf{u}^*_{n-1} \quad (14)$$

This subsection demonstrates that the latch approximation, used in (3) and (6), does not significantly impact the applied voltage vector, even for very high output frequency operations and machines with high values of saliency.

In order to validate the synchronous frame latch approximation, simulations are organized in the following way. A unit vector with an angle equal to $\Theta = 45\,\mathrm{deg}$ is used as the input to the following three matrices. The first one represents the simplified ZOH model, used in (3) and (6): $-\left(\mathbf{I} - e^{\mathbf{A}T_s}\right) \cdot \mathbf{A}^{-1} \cdot \mathbf{e}^{-j\frac{3}{2}\omega_e T_s}$. The second one represents the synchronous frame ZOH model with additional scalar gain, which is a combination of (3) and (14). The third matrix is the matrix $\mathbf{B} \cdot \mathbf{e}^{-j\omega_e T_s}$, which represents the exact voltage contribution in (13). The magnitude and angle errors, between the outputs of the first two matrices and the third matrix, are shown in Fig. 6.

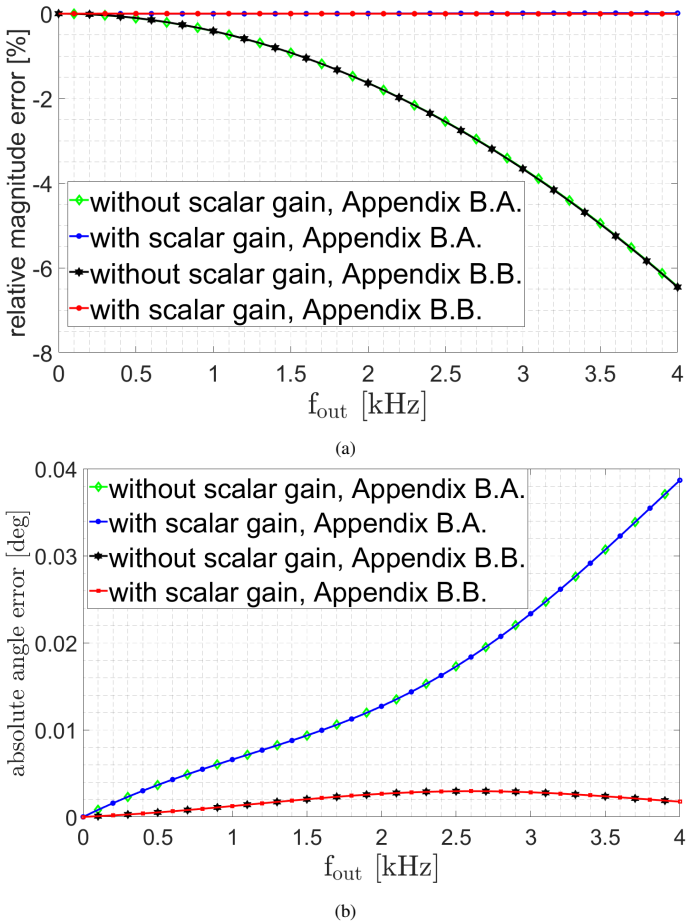

Fig. 6: Analysis of the synchronous frame ZOH approximation. The sampling frequency is equal to 20 kHz.

From Fig. 6, it is clear that the voltage latch approximation does not significantly impact the model accuracy, yet it greatly reduces its complexity. The magnitude error remains below 7% for output to sampling frequency ratios up to 0.2. This

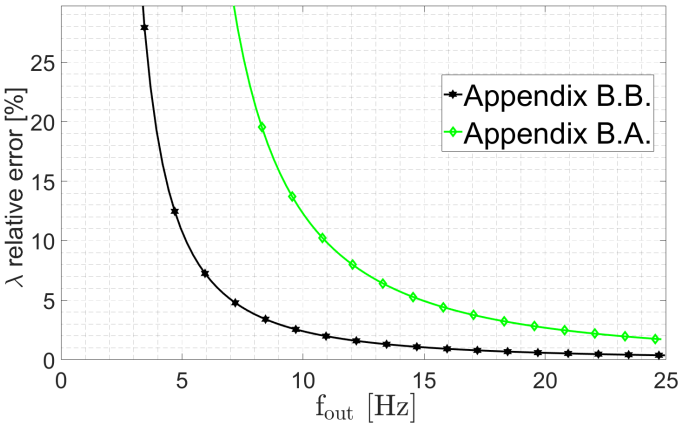

Fig. 7: Relative error between the magnitude of λ and ω_e.

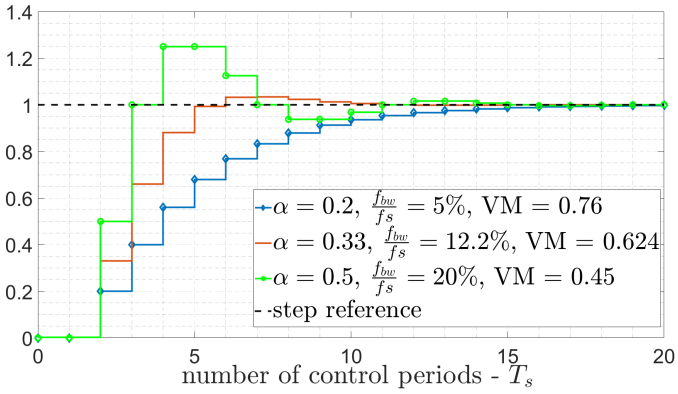

Fig. 8: The step response and closed-loop characteristics of $\mathbf{W}_{cl}$ for three values of parameter α.

error is practically nullified by including the scalar gain from (14), which is a simple modification of the proposed controller structure. The angle error is below 0.04 deg, for the mentioned output frequency range. It should be noted that the machine parameters have a certain impact only on the angle error.

B. Transformation of hyperbolic into sinusoidal functions

The second approximation, which is used to transform (4) into (8) is $\lambda = \sqrt{\delta^2 - \omega_e^2} \approx j\omega_e$. This approximation needs to be validated only for near-zero output frequencies, as ω_e^2 dominantly influences the value of λ starting from low-speed values.

For output frequencies $\omega_e < \delta$, the parameter λ is a real number. In that region, the argument λT_s of the hyperbolic functions in (4) is close to zero. Therefore, the Taylor expansion of hyperbolic functions is equal to the Taylor expansion of sinusoidal functions: $\cosh(\lambda T_s) \approx \cos(\lambda T_s) \approx 1$, $\sinh(\lambda T_s) \approx \sin(\lambda T_s) \approx \lambda T_s$, which justifies the use of sinusoidal functions instead of the hyperbolic ones.

For output frequencies $\omega_e > \delta$, the parameter λ is an imaginary number and therefore in (4), the hyperbolic functions are equal to the sinusoidal functions of the argument $Im\{\lambda T_s\}$. In this region, the approximation $Im\{\lambda\} \approx \omega_e$ is verified by calculating the relative error between the magnitudes of λ and ω_e. The results are shown in Fig. 7, for motors described in Appendix B.A and Appendix B.B. From Fig. 7, it could be wrongly concluded that this approximation produces significant modeling error in the low-speed region. However, the parameter λ in (4) is multiplied by T_s, which attenuates the error impact. Hence, the elements of matrix $e^{\mathbf{A}T_s}$ are not sensitive to this approximation. This is confirmed in subsection IV B where the results of the frequency response analysis and step responses are also provided for zero-speed and low-speed operations.

C. First-order approximation of sinusoidal function

The first-order approximation $\frac{\sin(\omega_e T_s)}{\omega_e} \approx T_s$ transforms (8) into (9). It does not depend on the motor parameters, and it simplifies $\delta\frac{\sin(\omega_e T_s)}{\omega_e}$ to δT_s. This approximation reduces the computation effort, as well as the numerical division problems for small values of ω_e. The relative error, equal to $\frac{2\pi\frac{f_{out}}{f_s} - \sin(2\pi\frac{f_{out}}{f_s})}{\sin(2\pi\frac{f_{out}}{f_s})}$, increases above 5% for $\frac{f_{out}}{f_s} > 8.5\%$. This approximation can be bypassed to increase the robustness of the derived controller at high speeds.

IV. Controller Design and Simulation Results

In this section, the closed-loop system shown in Fig. 4 is analyzed. The closed-loop analysis is used to calculate the controller parameter α based on the aimed response. The frequency response analyses of open-loop and closed-loop systems are performed to validate the derived plant model and controller structure. The proposed controller is then tested in order to verify the closed-loop step response for various operating modes. The results are presented for the output frequency ratios up to 0.2, for two different machines, described in Appendix B.A and Appendix B.B.

A. Closed-loop analysis and controller design

Based on (11), the open-loop transfer matrix of the system shown in Fig. 4, $\mathbf{W}_{ol}(z) = \mathbf{G}_{plant}(z) \cdot \mathbf{G}_{cf}(z)$ is equal to:

$$\mathbf{W}_{ol}(z) = \frac{\alpha}{z(z-1)}\mathbf{I} \tag{15}$$

The resulting closed-loop transfer matrix is equal to:

$$\mathbf{W}_{cl}(z) = \frac{\alpha}{z^2 - z + \alpha}\mathbf{I} \tag{16}$$

For the controller design, the closed-loop transfer matrix (16) is used to determine the gain α based on the desired closed-loop bandwidth and the allowed step response overshoot. Another important feature is the vector margin, which indicates robustness to model uncertainties [12], [15]–[17]. For industrial applications, the allowed current overshoot is usually limited under $(3-4)\%$ as it affects the design of the overcurrent protection. The value of 4% is taken as a design restriction in this paper. In Fig. 8, the step response of (16) is given for three different values of α. It can be seen that the loop with value $\alpha = 0.33$ results in a settling time of approximately $10\mathrm{T_s}$ and the overshoot of 3.47%, which fits in the design restriction. The complete list of parameters of the designed controller is shown in Table I.

TABLE I: Controller configuration and closed-loop characteristics

Controller parameters	Label	Value	unit
Controller gain	α	0.33	/
Sampling frequency	f_s	20	kHz
Closed-loop characteristics	**Label**	**Value**	**unit**
Bandwidth to sampling frequency ratio	$\frac{f_{bw}}{f_s}$	0.122	/
-3 dB bandwidth	f_{bw}	2443	Hz
Overshoot	OVSH	3.47	%
Vector margin	VM	0.624	/

For the direct comparison with the state-of-the-art methods, in the following analysis the closed-loop performance is evaluated for the current response, instead of the flux. The proposed controller from (12) is used in current control system by multiplying the current vectors with the inductance matrix, as seen in Fig. 3.

B. Frequency response analysis

The proposed controller structure is derived with the motivation to obtain the open-loop and closed-loop transfer matrices equal to (15) and (16), respectively. In order to ensure reliability, frequency responses of the current control loop are compared with (15) and (16). The simulations, performed in the MATLAB/Simulink environment, are organized in the following manner. The controller structure is implemented using discrete blocks, taking into account control-related delays. The Simulink abc frame machine model, supplied from a controlled voltage source, is used for two different machines, described in Appendix B.A and Appendix B.B. The control parameters are equal to those in Table I.

For Multiple-Input Multiple-Output (MIMO) systems, to which salient machines belong, the frequency response analysis is not straightforward as for the Single-Input Single-Output (SISO) systems [29]. However, since the coupling between the axes is handled by the controller, the cross-impact between the axes is negligible compared to the direct-impact of one axis on itself (the open-loop and closed-loop matrices are nearly diagonal). Due to this, for salient machines with properly structured controller, SISO frequency response provides useful information about the system. The justification of this is seen in the following subsection, where the step responses show no coupling between the axis. The frequency response analysis is performed for the closed-loop system in order to verify the -3 dB bandwidth, as well as for the open-loop system in order to verify the crossover frequency and the phase margin. For the analyzed axis current reference, sinusoidal perturbations of 0.1 A are superposed to the 2 A DC value. The reference current in the other axis is set to 0 A. The chosen number of settling periods is 2, and the number of estimation periods is 4. The perturbation frequencies are an arithmetic sequence starting from 100 Hz to 8850 Hz, with a step of 250 Hz. The response is tested for output to sampling frequency ratios of: $\{0, 0.045, 0.1, 0.2\}$. The results are shown in Fig. 9.

From results of the frequency response analysis, the following can be concluded. First of all, for output to sampling frequency ratios up to 0.1 the responses are in almost perfect match with the analytical transfer functions. A slight mismatch can be seen for the ratio of 0.2. Also, it can be seen that there is almost no difference between the frequency responses of d and q axes. Finally, the frequency response remains unaltered for the machine described in Appendix B.B, which has an extremely high value of saliency.

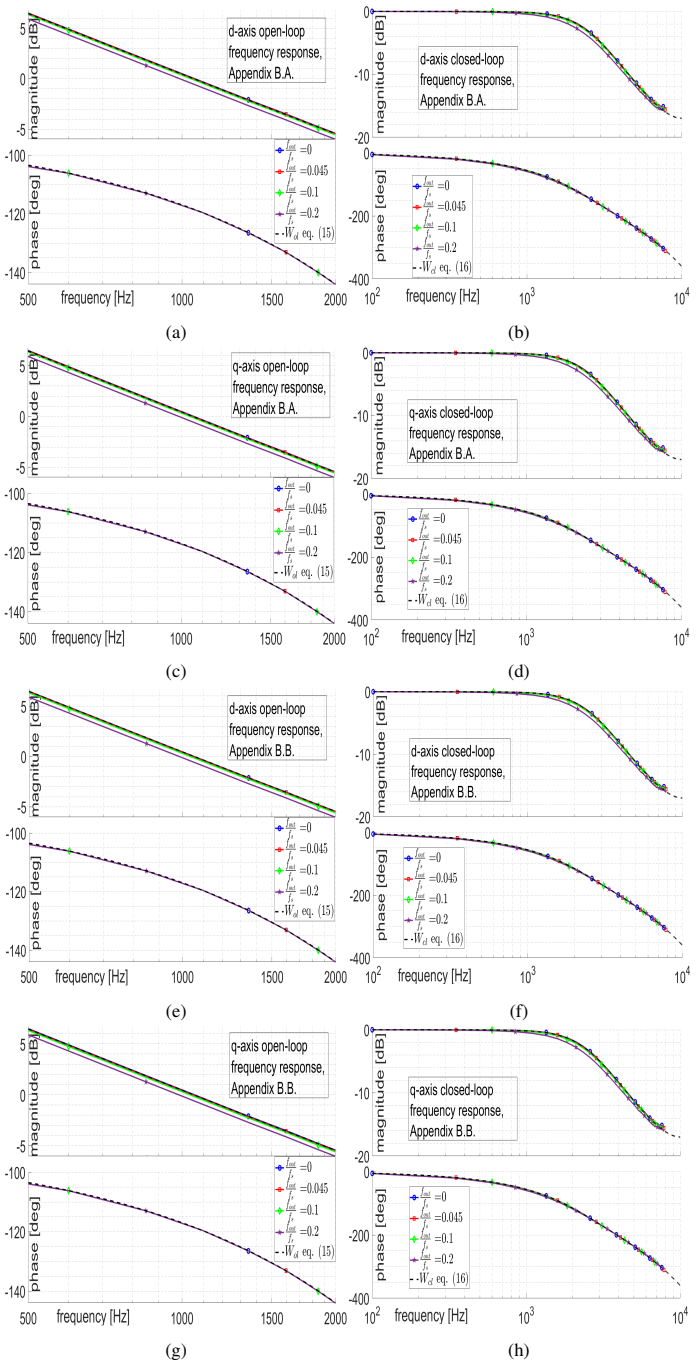

Fig. 9: The simulation results for the d and q axes frequency response analysis. The controller parameters are equal to the ones in Table I: (a) - (b) The open and closed-loop response for d-axis, machine in Appendix B.A; (c) - (d) The open and closed-loop response for q-axis, machine in Appendix B.A; (e) - (f) The open and closed-loop response for d-axis, machine in Appendix B.B; (g) - (h) The open and closed-loop response for q-axis, machine in Appendix B.B.

C. Step response of the closed-loop system

The goal of this subsection is to show the following:

- The machine described in Appendix B.A, which is used in the experimental tests, features high-enough saliency for the dq axes currents to have significantly different dynamics.
- Controllers that rely on continuous-time approximations, such as the PI with axes decoupling terms, do not offer satisfactory performance starting from moderate output frequencies.
- The comparison between the step responses of the simulated current loop and the theoretical one - $\mathbf{W}_{cl}(z)$ (16).
- The proposed controller structure enables the current loop to maintain robustness for very high output frequencies, while being tuned to a very high bandwidth $\frac{f_{bw}}{f_s} = 0.122$. The simulation results are given for the output frequency ratios up to $\frac{f_{out}}{f_s} = 0.15$.
- The proposed controller is able to achieve the decoupling of the axes dynamics for high output frequency ratios and highly salient machines. The results are given for the SynRel machine, described in Appendix B.B, which has a very high value of saliency, reaching a maximum of $\frac{L_d}{L_q} = 18.6$.

The simulation model is the same as the one used for the frequency response analysis. The current loop step response is tested for quick square-pulse references in both axes. The pulse magnitudes are 2.5 A, and the pulse duration is 2.5 ms. The response is tested for output frequencies from 0 Hz to 3 kHz. The simulation results are sampled with a rate equal to T_s and plotted in MATLAB, with a focus on rising and falling edges of the square pulses. In all conducted simulations, controller parameters are equal to the ones in Table I.

The most often used structure for current control in industrial drives is a two-axis PI controller with axes decoupling terms and output voltage angle compensation [6], [7], [30]. This kind of controller can be designed as the IMC in continuous-time domain [5]. The proportional gain in each axis is equal to $\alpha f_s L_{dq}$, where α is the relative bandwidth and L_{dq} is the respective axis inductance. The integral gain is equal to $\alpha f_s R$. In order to decouple the axes dynamics, state-feedback term $\mp\omega_e L_{dq} i_{dq}$ is added to the output of the respective axis PI controller. For the compensation of the control-related time delays, the voltage reference is rotated by $\frac{3}{2}\omega_e T_s$ in the positive direction. The performance of the above described PI current controller is compared to the controller proposed in this paper. For a fair comparison, the loop gain α is the same for both controllers. The results are shown in Fig. 10, for the machine described in Appendix B.A and the output frequency equal to 150 Hz. The results show that the commonly used PI controller does not provide decoupling of the axes dynamics, even at moderate output frequency of 150 Hz. Even worse performance is obtained when the controller is applied for machines with higher values of saliency. As stated in [12], the implementation of a PI controller with state-feedback axes decoupling terms, causes the closed-loop poles to migrate as the frequency increases, making them lightly damped. This causes the system behaviour to become highly

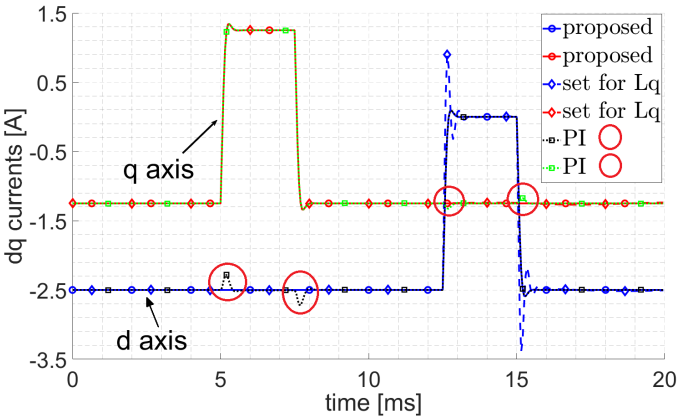

Fig. 10: Simulation results for the machine in Appendix B.A and output frequency equal to $f_{out} = 150$ Hz. The comparison between the proposed controller, the discrete IMC for non-salient machines with gains set to $L = L_q$, and the PI controller with state-feedback decoupling terms. All controllers feature the same value of gain $\alpha = 0.33$.

oscillatory when operating at high synchronous frequencies. Additional simulation results for the PI controller are not shown in this paper, but as the frequency increases, the axes coupling becomes intolerably high, and the loop loses stability for $\frac{f_{out}}{f_s} > 0.142$. Detailed performance and stability analyses of continuous and discrete based current controllers can be found in [12].

As stated in [25], for machines with low values of saliency ($L_d \approx L_q$), satisfactory performance is achieved by implementing the discrete IMC for non-salient machines [12], [15]–[17]. In that case, the value L is replaced with an inductance value between L_d and L_q. However, as the saliency increases, the current in the higher-inductance axis features a slower response compared to the current in the lower-inductance axis. The implementation of this kind of controller can lead to a lightly damped oscillatory response in the lower-inductance axis. The worst-case scenario is when the non-salient discrete IMC is tuned according to the higher-inductance value ($L = L_q$). For such tuning and the machine described in Appendix B.A, the current loop step response is shown in Fig. 10. The presented result confirms that the machine from Appendix B.A has high enough saliency for the experimental verification of the proposed controller structure.

The current loop step responses, for the proposed controller, are further simulated and compared to the step response of (16). The results are shown in Fig. 11 and Fig. 12, for the machines decribed in Appendix B.A. and Appendix B.B, respectively.

The excellent match between the step responses of (16) and the simulated current loop shows that the derived plant model $\mathbf{G}_{plant}$ is accurate and that the controller $\mathbf{G}_{cf}$ is capable of decoupling the axes dynamics. The results for a very high output frequency ratio $\frac{f_{out}}{f_s} = 0.15$ show a negligible mismatch from the theoretical response. The excellent agreement between the results for both machines leads to the same conclusion as the one from the frequency response analysis: the proposed current loop is not affected by the value of machine saliency.

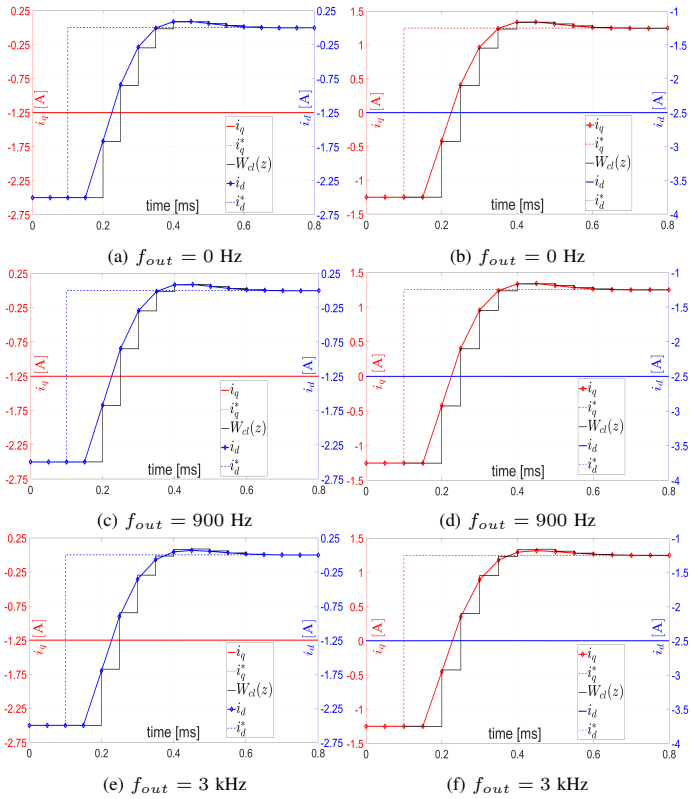

(a) $f_{out} = 0$ Hz (b) $f_{out} = 0$ Hz

(c) $f_{out} = 900$ Hz (d) $f_{out} = 900$ Hz

(e) $f_{out} = 3$ kHz (f) $f_{out} = 3$ kHz

Fig. 11: The simulation results for the dq axes current step responses, for the machine described in Appendix B.A. The controller parameters are equal to the ones in Table I.

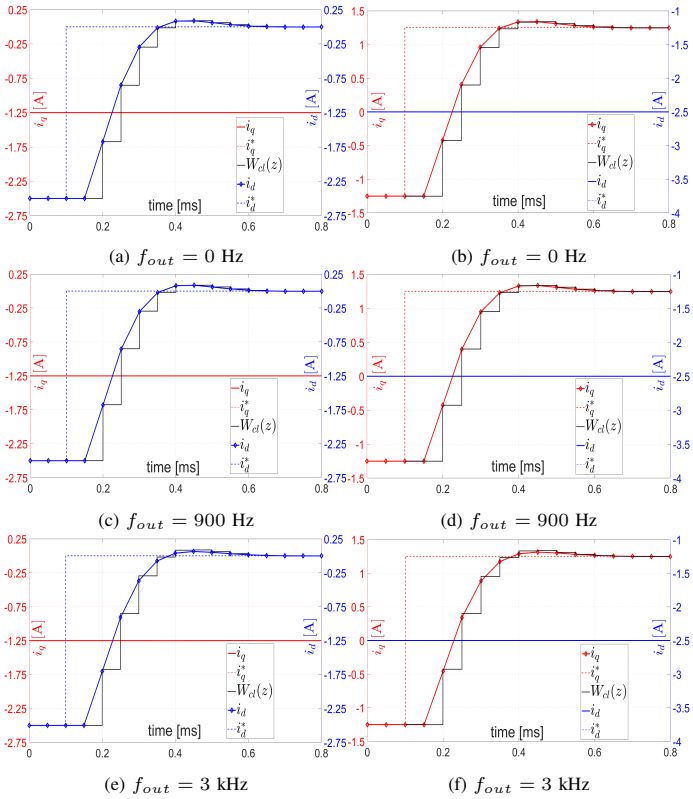

(a) $f_{out} = 0$ Hz (b) $f_{out} = 0$ Hz

(c) $f_{out} = 900$ Hz (d) $f_{out} = 900$ Hz

(e) $f_{out} = 3$ kHz (f) $f_{out} = 3$ kHz

Fig. 12: The simulation results for the dq axes current step responses, for the machine described in Appendix B.B. The controller parameters are equal to the ones in Table I.

V. Experimental Results

For experimental verification of the proposed controller the algorithm is implemented on a DSP based platform, which uses the TMS320F28335 device. The experimental results are presented for a synchronous motor with surface-mounted magnets. The motor is supplied by an industrial PWM-controlled IGBT inverter with the switching frequency $f_{pwm} = 10$ kHz [31]. The machine and drive parameters are shown in Appendix B.A. The current is acquired using ADC peripheral and on-chip direct memory access (DMA) unit. The implemented sampling method is synchronous double sampling with the frequency $f_s = 20$ kHz. The experimental setup is shown in Fig. 13.

For the experimental tests, the current references are set in the same manner as for the simulations, and the measurements are acquired with the period equal to $T_s = \frac{1}{2}T_{pwm}$. The waveforms are compared to the theoretical step response - $\mathbf{W}_{cl}(z)$ (16). The current response is tested for speeds up to 18 krpm due to the mechanical constraints of the experimental setup. For tests at speeds higher than 9 krpm, the magnets are taken out of the rotor. For the experimental tests shown in Fig. 14 and Fig. 15, the controller parameters are equal to the ones in Table I. The relative closed-loop bandwidth is equal to $\frac{f_{bw}}{f_s} = 12.2\%$, which corresponds to $f_{bw} = 2443$ Hz. These results are presented for the output frequency ratios up to $\frac{f_{out}}{f_s} = 4.5\%$. In order to test the controller at higher values of $\frac{f_{out}}{f_s}$, the switching frequency is decreased to 5 kHz and 2.5 kHz. The sampling frequency is also decreased to $2f_{pwm}$. For

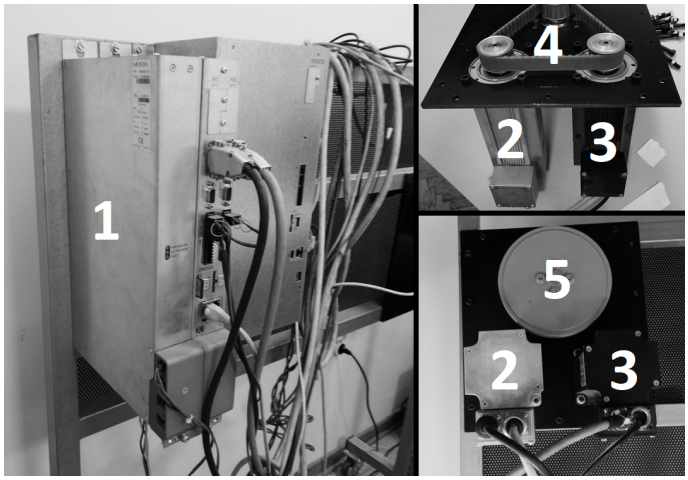

Fig. 13: The experimental setup with a six-pole synchronous permanent-magnet motor: (1) Two-axes module comprising two 3-phase inverters and control circuits. The PC-based GUI connection is established using EtherCat link. (2) The motor under the test. (3) Speed-controlled motor. (4) Toothed belt coupling for two motors and inertia. (5) Inertia.

those experimental results, shown in Fig. 16, the controller gain remains equal to $\alpha = 0.33$, which retains the relative bandwidth equal to $\frac{f_{bw}}{f_s} = 12.2\%$.

The first result, shown in Fig. 14, presents current loop step responses for the proposed controller with gains calculated according to L_q and the output frequency of 150 Hz. This result matches the one from Fig. 10 and demonstrates that the machine from Appendix B.A has high enough saliency for the

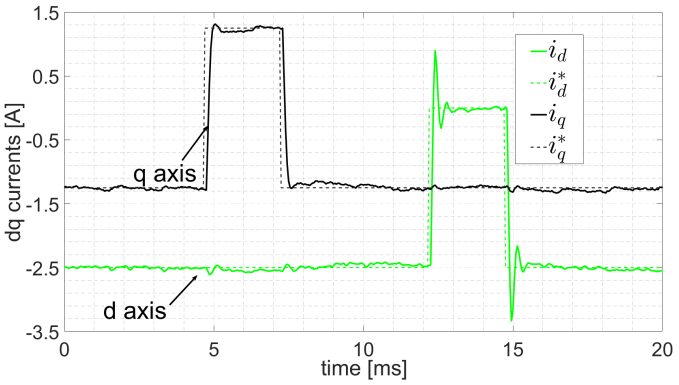

Fig. 14: The experimental result for the proposed controller with gains set according to L_q. The parameter $\alpha = 0.33$, the sampling frequency is 20 kHz, and the output frequency is $f_{out} = 150$ Hz.

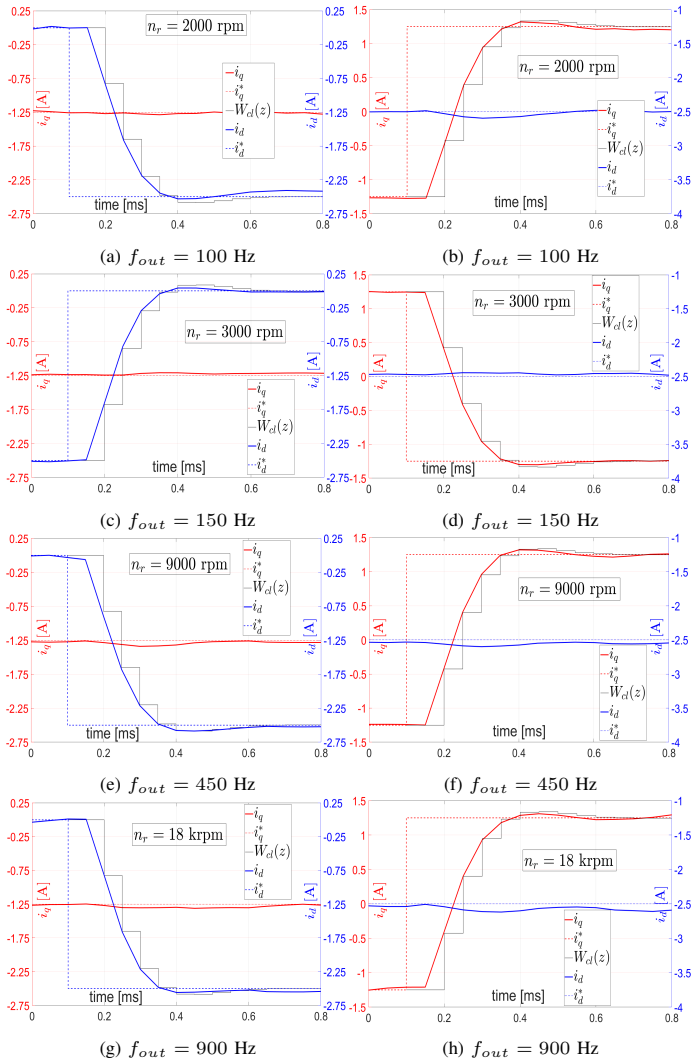

(a) $f_{out} = 100$ Hz (b) $f_{out} = 100$ Hz

(c) $f_{out} = 150$ Hz (d) $f_{out} = 150$ Hz

(e) $f_{out} = 450$ Hz (f) $f_{out} = 450$ Hz

(g) $f_{out} = 900$ Hz (h) $f_{out} = 900$ Hz

Fig. 15: The experimental results for the d and q axes current responses, for the machine in Appendix B.A. The switching frequency is equal to 10 kHz. The controller parameters are shown in Table I.

verification of the proposed controller.

The following results, shown in Fig. 15, verify the proposed controller for various rotational speeds. The current loop is tested for rotor speeds equal to 2 krpm, 3 krpm, 9 krpm, and 18

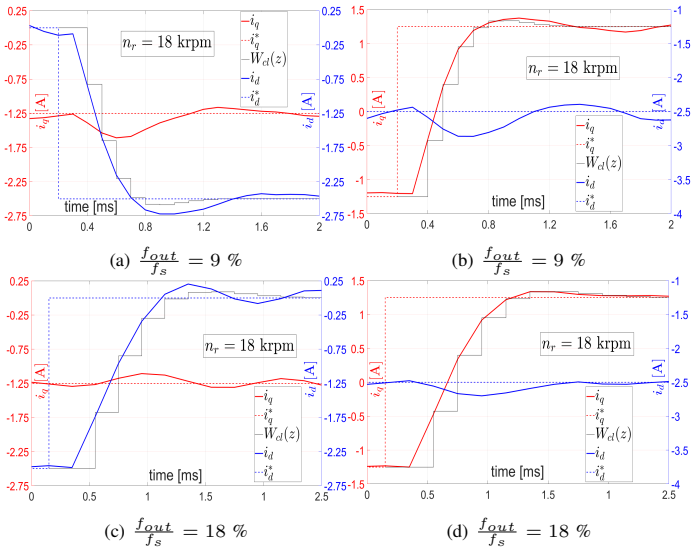

(a) $\frac{f_{out}}{f_s} = 9$ % (b) $\frac{f_{out}}{f_s} = 9$ %

(c) $\frac{f_{out}}{f_s} = 18$ % (d) $\frac{f_{out}}{f_s} = 18$ %

Fig. 16: The experimental results for the d and q axes current responses, for the machine in Appendix B.A. The value of controller parameter α is the same as for the previous tests, equal to 0.33: (a) - (b) The switching frequency is equal to 5 kHz; (c) - (d) The switching frequency is equal to 2.5 kHz.

krpm, which correspond to the output frequencies of 100 Hz, 150 Hz, 450 Hz, and 900 Hz, respectively. From the presented step responses, it can be seen that the experimental results are in an excellent agreement with the theoretical response and that the step response does not deteriorate with the increase of the output frequency. The presented results verify that the controller is capable to achieve the constant dynamics in both axes, and a decoupled response. A slight mismatch from the step response of (16) and low-magnitude oscillations are present, contrary to the simulation results. This is due to the spectral aliasing and current acquisition errors related to the implemented sampling method. It is well analyzed in [15] that the synchronous sampling cannot provide the zero-error feedback acquisition, due to LC parasitics, anti-aliasing filter, lockout time, and other effects. For increased robustness, advanced oversampling techniques are becoming a standard for feedback acquisition.

The results with reduced switching frequency, shown in Fig. 16, demonstrate that the proposed controller structure is able to maintain a stable current response up to a very high output to sampling frequency ratio $\frac{f_{out}}{f_s} = 18\%$, while being tuned to a very high relative bandwidth $\frac{f_{bw}}{f_s} = 12.2\%$. As noted in section III, some of the modelling approximations can be avoided in order to reduce errors at very high output frequencies. However, it was of interest to show that with all approximations, the proposed controller maintains a stable response at $\frac{f_{out}}{f_s} = 18\%$. The results for the decreased switching frequency show higher axes coupling, yet the step response is still in good agreement with the theoretical one. It should be noted that, with the decrease of the switching frequency, the current ripple significantly increases, which, without doubt impacts the current response in the presented results.

The directly comparable state-of-the-art methods for salient machines are [13] and [26]. The experimental results in [13]

report the maximal output frequency ratio equal to $\frac{f_{out}}{f_s} = 0.1$, for the loop tuned to $\frac{f_{bw}}{f_s} = 0.05$. In [13], the results show low-magnitude oscillations and slight axes coupling in step responses. The experimental results in [26] report the maximal output frequency ratio of $\frac{f_{out}}{f_s} = 0.12$, for the loop tuned to $\frac{f_{bw}}{f_s} \approx 0.07$. The results show severe output oscillations and the axes coupling is not presented for high output frequencies.

The experimental results in this paper present the maximal value of output frequency ratio equal to $\frac{f_{out}}{f_s} = 0.18$, for the loop bandwidth ratio equal to $\frac{f_{bw}}{f_s} = 0.122$. The capability to maintain the loop stability and to provide nearly theoretical current step response, for these values of output frequency and bandwidth, demonstrates the effectiveness of the proposed controller.

VI. Conclusion

This paper has presented a novel structure of current controller for salient machines. The proposed controller is compact and offers a very robust response. The simulation results have demonstrated its capability to decouple the axes dynamics for high output frequencies, high bandwidth and for machines with very high value of saliency. The experimental results have verified the current loop response for relative values of bandwidth and output frequency higher than the state-of-the-art methods. In order to further improve robustness, oversampling based methods for feedback acquisition should be investigated. Most importantly, for highly non-linear machines such as SynRel, the adaptive control should be investigated, with the motivation to maintain constant current loop dynamics for all operating points.

Appendix A
Derivation of the flux controller

The flux controller is derived by substituting (10) into (11), which subsequently expands to (17). In order to obtain a more compact structure of the controller, the following matrix from (17), $\mathbf{W} = (\mathbf{I} - \mathbf{E})^{-1} \cdot \left(\mathbf{I} - \frac{1}{z}\mathbf{E}\right) = \frac{1}{\xi}\begin{bmatrix} w_{11} & w_{12} \\ w_{21} & w_{22} \end{bmatrix}$ is further analyzed.

The exact value of the denominator ξ is shown in (18). With the following approximations: $\sin^2(\omega_e T_s) \approx \omega_e^2 T_s^2$, $e^{\sigma T_s} \approx 1 + \sigma T_s$, and $\cos(\omega_e T_s) \approx 1$, the parameter ξ is transformed into (19). The denominator ξ is repositioned to the beginning of the controller, as shown in Fig. 5. The remaining elements of the matrix $\mathbf{W}$, shown in (20), are regrouped to obtain a compact form shown in (21).

Appendix B
Machine and Drive Configuration

A. Experimentally used motor

PMSM with Surface-Mounted Magnets	Label	Value	unit
Rated RMS current	I_n	7.3	A
Rated RMS line voltage	U_n	400	V
Rated frequency	f_n	240	Hz
Rated speed	n_n	4800	rpm
d-axis inductance	L_d	7.6	mH
q-axis inductance	L_q	12.9	mH
Stator resistance	R_s	1.057	Ω
PM flux magnitude	Ψ_{pm}	0.2	Wb
Number of poles	$2p$	6	/
Industrial IGBT Inverter	**Label**	**Value**	**unit**
Switching frequency	f_{pwm}	10	kHz
Sampling period	T_s	50	μs
Lockout time (compensated)	t_{dt}	2.8	μs
DC bus voltage	V_{dc}	650	V

B. Highly salient industrial SynRel motor

Synchronous Reluctance	Label	Value	unit
d-axis inductance	L_d	65	mH
q-axis inductance	L_q	3.5	mH
Stator resistance	R_s	0.1	Ω
Number of poles	$2p$	4	/

References

[1] D. W. Novotny and T. A. Lipo, *Vector control and dynamics of AC drives*. Oxford university press, 1996, vol. 1.

[2] M. P. Kazmierkowski and L. Malesani, "Current control techniques for three-phase voltage-source pwm converters: a survey," *IEEE Transactions on Industrial Electronics*, vol. 45, no. 5, pp. 691–703, Oct 1998.

[3] D. G. Holmes, B. P. McGrath, and S. G. Parker, "Current regulation strategies for vector-controlled induction motor drives," *IEEE Transactions on Industrial Electronics*, vol. 59, no. 10, pp. 3680–3689, Oct 2012.

[4] T. M. Rowan and R. J. Kerkman, "A new synchronous current regulator and an analysis of current-regulated pwm inverters," *IEEE Transactions on Industry Applications*, vol. IA-22, no. 4, pp. 678–690, July 1986.

[5] L. Harnefors and H. . Nee, "Model-based current control of ac machines using the internal model control method," *IEEE Transactions on Industry Applications*, vol. 34, no. 1, pp. 133–141, Jan 1998.

[6] A. G. Yepes, A. Vidal, J. Malvar, O. López, and J. Doval-Gandoy, "Tuning method aimed at optimized settling time and overshoot for synchronous proportional-integral current control in electric machines," *IEEE Transactions on Power Electronics*, vol. 29, no. 6, pp. 3041–3054, June 2014.

[7] F. D. Freijedo, A. Vidal, A. G. Yepes, J. M. Guerrero, . López, J. Malvar, and J. Doval-Gandoy, "Tuning of synchronous-frame pi current controllers in grid-connected converters operating at a low sampling rate by mimo root locus," *IEEE Transactions on Industrial Electronics*, vol. 62, no. 8, pp. 5006–5017, Aug 2015.

[8] F. Briz, M. W. Degner, and R. D. Lorenz, "Analysis and design of current regulators using complex vectors," *IEEE Transactions on Industry Applications*, vol. 36, no. 3, pp. 817–825, May 2000.

[9] J. Holtz, Juntao Quan, J. Pontt, J. Rodriguez, P. Newman, and H. Miranda, "Design of fast and robust current regulators for high-power drives based on complex state variables," *IEEE Transactions on Industry Applications*, vol. 40, no. 5, pp. 1388–1397, Sep. 2004.

[10] Hyunbae Kim and R. D. Lorenz, "Synchronous frame pi current regulators in a virtually translated system," in *Conference Record of the 2004 IEEE Industry Applications Conference, 2004. 39th IAS Annual Meeting.*, vol. 2, Oct 2004, pp. 856–863 vol.2.

[11] K. Huh and R. D. Lorenz, "Discrete-time domain modeling and design for ac machine current regulation," in *2007 IEEE Industry Applications Annual Meeting*, Sep. 2007, pp. 2066–2073.

[12] H. Kim, M. W. Degner, J. M. Guerrero, F. Briz, and R. D. Lorenz, "Discrete-time current regulator design for ac machine drives," *IEEE Transactions on Industry Applications*, vol. 46, no. 4, pp. 1425–1435, July 2010.

[13] M. Hinkkanen, H. Asad Ali Awan, Z. Qu, T. Tuovinen, and F. Briz, "Current control for synchronous motor drives: Direct discrete-time pole-placement design," *IEEE Transactions on Industry Applications*, vol. 52, no. 2, pp. 1530–1541, March 2016.

[14] N. Hoffmann, F. W. Fuchs, M. P. Kazmierkowski, and D. Schröder, "Digital current control in a rotating reference frame - part i: System modeling and the discrete time-domain current controller with improved decoupling capabilities," *IEEE Transactions on Power Electronics*, vol. 31, no. 7, pp. 5290–5305, July 2016.

[15] S. N. Vukosavić, L. S. Perić, and E. Levi, "Ac current controller with error-free feedback acquisition system," *IEEE Transactions on Energy Conversion*, vol. 31, no. 1, pp. 381–391, March 2016.

[16] ——, "A three-phase digital current controller with improved performance indices," *IEEE Transactions on Energy Conversion*, vol. 32, no. 1, pp. 184–193, March 2017.

[17] ——, "Digital current controller with error-free feedback acquisition and active resistance," *IEEE Transactions on Industrial Electronics*, vol. 65, no. 3, pp. 1980–1990, March 2018.

[18] X. Zhang, G. H. B. Foo, D. M. Vilathgamuwa, and D. L. Maskell, "An improved robust field-weakeaning algorithm for direct-torque-controlled synchronous-reluctance-motor drives," *IEEE Transactions on Industrial Electronics*, vol. 62, no. 5, pp. 3255–3264, May 2015.

[19] G. Zhang, G. Wang, D. Xu, and Y. Yu, "Discrete-time low-frequency-ratio synchronous-frame full-order observer for position sensorless ipmsm drives," *IEEE Journal of Emerging and Selected Topics in Power Electronics*, vol. 5, no. 2, pp. 870–879, June 2017.

[20] E. Trancho, E. Ibarra, A. Arias, I. Kortabarria, J. Jurgens, L. Marengo, A. Fricassè, and J. V. Gragger, "Pm-assisted synchronous reluctance machine flux weakening control for ev and hev applications," *IEEE Transactions on Industrial Electronics*, vol. 65, no. 4, pp. 2986–2995, April 2018.

[21] Y. Bao, M. Degano, S. Wang, L. Chuan, H. Zhang, Z. Xu, and C. Gerada, "A novel concept of ribless synchronous reluctance motor for enhanced torque capability," *IEEE Transactions on Industrial Electronics*, vol. 67, no. 4, pp. 2553–2563, April 2020.

[22] Hyung-Tae Moon, Hyun-Soo Kim, and Myung-Joong Youn, "A discrete-time predictive current control for pmsm," *IEEE Transactions on Power Electronics*, vol. 18, no. 1, pp. 464–472, Jan 2003.

[23] C. Lin, J. Yu, Y. Lai, and H. Yu, "Improved model-free predictive current control for synchronous reluctance motor drives," *IEEE Transactions on Industrial Electronics*, vol. 63, no. 6, pp. 3942–3953, June 2016.

[24] R. Antonello, M. Carraro, L. Peretti, and M. Zigliotto, "Hierarchical scaled-states direct predictive control of synchronous reluctance motor drives," *IEEE Transactions on Industrial Electronics*, vol. 63, no. 8, pp. 5176–5185, Aug 2016.

[25] A. Altomare, A. Guagnano, F. Cupertino, and D. Naso, "Discrete-time control of high speed salient machines," in *2014 IEEE Energy Conversion Congress and Exposition (ECCE)*, Sep. 2014, pp. 3528–3534.

[26] ——, "Discrete-time control of high-speed salient machines," *IEEE Transactions on Industry Applications*, vol. 52, no. 1, pp. 293–301, Jan 2016.

[27] C. M. Hackl, M. J. Kamper, J. Kullick, and J. Mitchell, "Current control of reluctance synchronous machines with online adjustment of the controller parameters," in *2016 IEEE 25th International Symposium on Industrial Electronics (ISIE)*, June 2016, pp. 153–160.

[28] Bon-Ho Bae and Seung-Ki Sul, "A compensation method for time delay of full-digital synchronous frame current regulator of pwm ac drives," *IEEE Transactions on Industry Applications*, vol. 39, no. 3, pp. 802–810, May 2003.

[29] S. Skogestad and I. Postlethwaite, *Multivariable feedback control: analysis and design*. Wiley New York, 2007, vol. 2.

[30] J. Yim, S. Sul, B. Bae, N. R. Patel, and S. Hiti, "Modified current control schemes for high-performance permanent-magnet ac drives with low sampling to operating frequency ratio," *IEEE Transactions on Industry Applications*, vol. 45, no. 2, pp. 763–771, March 2009.

[31] DM2020 Data Manual, MOOG Italiana S.r.l., Casella, Italy, 2011.

Ivan Z. Petric (S'20) was born in Belgrade, Serbia, in 1994. He received the B.S. and M.S. degrees in Electrical Engineering from the University of Belgrade, Belgrade, Serbia, in 2017 and 2018, respectively.

From 2018 to 2019, he was a Researcher with the the Power Electronics, Machines and Control Group, The University of Nottingham, U.K. He is currently pursuing the Ph.D. degree with the Power Electronics Group, Department of Information Engineering, University of Padova, Italy. His research interests include digital control of electrical drives and grid connected converters, smart microgrids, and renewable energy sources.

Equations used in Appendix A

$$\mathbf{G}_{cf}(z) = \alpha \frac{z}{z-1} \frac{1}{z^2} \mathbf{G}_{plant}^{-1}(z) = -\alpha \frac{z}{z-1} \frac{1}{z} \mathbf{e}^{j\frac{3}{2}\omega_e T_s} \cdot \mathbf{A} \cdot (\mathbf{I} - \mathbf{E})^{-1} \cdot (z\mathbf{I} - \mathbf{E}) = \alpha \frac{z}{z-1} \mathbf{e}^{j\frac{3}{2}\omega_e T_s} \cdot (-\mathbf{A}) \cdot \mathbf{W} \tag{17}$$

$$\xi = e^{-\sigma T_s} \left[1 - 2e^{\sigma T_s} \cos(\omega_e T_s) + e^{2\sigma T_s} - T_s^2 \delta^2 \right] = e^{-\sigma T_s} \left[\left(e^{\sigma T_s} - \cos(\omega_e T_s) \right)^2 + \sin^2(\omega_e T_s) - T_s^2 \delta^2 \right] \tag{18}$$

$$\xi \approx e^{-\sigma T_s} \left(\omega_e^2 + \frac{R^2}{L_d L_q} \right) T_s^2 \tag{19}$$

$$\begin{aligned} w_{11} &= -\cos(\omega_e T_s) - T_s \delta + e^{\sigma T_s} + \left(-\cos(\omega_e T_s) + T_s \delta + (1 - T_s^2 \delta^2) e^{-\sigma T_s} \right) z^{-1} \\ w_{12} &= \sin(\omega_e T_s) - \sin(\omega_e T_s) z^{-1} \\ w_{21} &= -\sin(\omega_e T_s) + \sin(\omega_e T_s) z^{-1} \\ w_{22} &= -\cos(\omega_e T_s) + T_s \delta + e^{\sigma T_s} + \left(-\cos(\omega_e T_s) - T_s \delta + (1 - T_s^2 \delta^2) e^{-\sigma T_s} \right) z^{-1} \end{aligned} \tag{20}$$

$$\xi \mathbf{W} = e^{\sigma T_s} \mathbf{I} - \mathbf{e}^{j\omega_e T_s} + z^{-1} \left[(1 - T_s^2 \delta^2) e^{-\sigma T_s} \mathbf{I} - \mathbf{e}^{-j\omega_e T_s} \right] + T_s \delta \begin{bmatrix} -1 & 0 \\ 0 & 1 \end{bmatrix} \left(1 - z^{-1} \right) \tag{21}$$

Slobodan N. Vukosavic (M'93, SM'12) was born in Sarajevo, Yugoslavia, in 1962. He received the B.S., M.S., and Ph.D. degrees from the University of Belgrade, Belgrade, Yugoslavia, in 1985, 1987, and 1989, respectively, all in Electrical Engineering. He was with the Nikola Tesla Institute, Belgrade, Yugoslavia, until 1988, when he joined the ESCD Laboratory of Emerson Electric, St. Louis, MO. Since 1991, he worked with Vickers Electric Company and MOOG Electric. S.N. Vukosavic is with the Department of Electrical Engineering, The University of Belgrade, and Serbian Academy of Sciences and Arts.

His interests include digital control, power conversion in renewable energy sources and power quality. He has published over 100 papers, 4 textbooks and 7 monographs and has completed over 42 large R/D and industrial projects.

Michele Degano (M'15) received the Laurea degree in electrical engineering from the University of Trieste, Trieste, Italy, in 2011, and the Ph.D. degree in industrial engineering from the University of Padova, Padova, Italy, in 2015. During his doctoral studies, he cooperated with several companies for the design of permanent-magnet machines. In 2015, he joined the Power Electronics, Machines and Control Group, The University of Nottingham, Nottingham, U.K., where he is currently an Associate Professor teaching advanced courses on electrical machines.

His main research interests include analysis, design of electrical machines, permanent-magnet machines, reluctance and permanent-magnet-assisted synchronous reluctance motors, and their optimisation through genetic algorithms. He is currently leading a number of industrial research projects for automotive and aerospace applications, ranging from small to large power, with focus on development of future hybrid electric aerospace and platforms for electrification of transports.

Alessandro Galassini (S'13-M'17) received the Master's degree in Mechatronic Engineering in 2012 from the University of Modena and Reggio Emilia, Reggio Emilia, Italy. In 2017, he received the Ph.D. degree in power sharing for multi-three-phase electrical machines from the University of Nottingham, Nottingham, U.K. Currently, he is a Researcher with the Power Electronics, Machines and Control Group group, The University of Nottingham, Nottingham, U.K., and his research area is focused on control of electrical drives for future transportation systems.